

# A New Method For Galaxy Cluster Detection I: The Algorithm

Michael D. Gladders

*and*

H.K.C. Yee

*Department of Astronomy, University of Toronto, 60 St. George St., Toronto, ON, M5S 3H8, Canada*

## ABSTRACT

Numerous methods for finding clusters at moderate to high redshifts have been proposed in recent years, at wavelengths ranging from radio to X-rays. In this paper we describe a new method for detecting clusters in two-band optical/near-IR imaging data. The method relies upon the observation that all rich clusters, at all redshifts observed so far, appear to have a red sequence of early-type galaxies. The emerging picture is that all rich clusters contain a core population of passively evolving elliptical galaxies which are coeval and formed at high redshifts. The proposed search method exploits this strong empirical fact by using the red sequence as a direct indicator of overdensity. The fundamental advantage of this approach is that with appropriate filters, cluster elliptical galaxies at a given redshift are redder than all normal galaxies at lower redshifts. A simple color cut thus virtually eliminates all foreground contamination, even at significant redshifts. In this paper, one of a series of two, we describe the underlying assumptions and basic techniques of the method in detail, and contrast the method with those used by other authors. We provide a brief demonstration of the effectiveness of the technique using real redshift data, and from this conclude that the method offers a powerful yet simple way of identify galaxy clusters.

*Subject headings:* methods: data analysis – galaxies: clusters: general

## 1. Introduction

The detection and characterization of rich clusters of galaxies at moderate ( $z \sim 0.5$ ) to high ( $z \gtrsim 1.0$ ) redshifts provides a crucial test of both cosmological models (e.g., Carlberg et al. 1996; Carlberg et al. 1997a; Fan, Bahcall, & Cen 1997; Oukbir & Blanchard 1997; Bahcall & Fan 1998; Ledlow et al. 1999) and galaxy evolution (e.g., Gladders et al. 1998; Kodama et al. 1998; Stanford, Eisenhardt, & Dickinson 1998, hereafter SED98). Clusters trace structure in the Universe to large scales (e.g., Gramann et al. 1995; Tadros, Efstathiou, & Dalton 1998), and provide many examples of both strong and weak lensing (e.g., Gioia & Luppino 1994; Kaiser 1995; Clowe et al. 1998; Luppino et al. 1999). The obvious importance of galaxy clusters has led to numerous galaxy cluster surveys in recent years, in many wavebands (e.g., the Palomar Distant Cluster Survey, Postman et al. 1996; the ROSAT Distant Cluster Survey, Rosati et al. 1998). As pointed out by Kepner et al. (1999), each of these surveys has defined its own detection algorithm, considered by the individual authors to be appropriate to their particular data. In essence, each of these detection algorithms makes assumptions about “what a cluster looks like” and then searches the relevant data to identify likely cluster locations.

All cluster finding methods suffer from selection effects. At minimum, each will be biased against any clusters which do not fit the particular cluster definition used. X-ray surveys, which ultimately define clusters as diffuse X-ray sources, are potentially biased against gas-poor clusters, and clusters in which the gas distribution is compact and hence unresolved. There is some evidence for optically rich and massive, but X-ray weak clusters. For example, Bower et al. (1994) found that a sample of 14 optically selected rich clusters at  $z \sim 0.4$  showed relatively weak X-ray emission. Castander et al. (1994) found similar results for a sample of optically selected clusters at  $z \sim 0.8$ . Optical surveys are potentially biased against optically dark clusters – deep cluster-sized potential wells which, for whatever reason, have failed to form a significant galaxy population. Notably, there is little evidence for many such clusters. The X-ray selected sample of Vikhlinin et al. (1998) showed no evidence for any optically dark clusters, with a sample of  $\sim 200$  X-ray selected clusters from  $z = 0.015$  to  $z > 0.5$ . More recently, the cluster AXJ2019+112 at

$z = 1.01$ , claimed by Hattori et al. (1997) to be a dark cluster, has been shown by Benítez et al. (1999) to not be dark at all. Clusters which are under-luminous in galaxian light may exist, but appear to be the exception rather than the norm.

More complicated redshift dependent biases and uncertainties also exist in most cluster catalogs, quite apart from the dominant cosmological effects of redshift. For example, the extreme bright end of the X-ray cluster luminosity function may be evolving negatively with redshift, and is poorly constrained at  $z > 1$  (Rosati et al. 1998). Similarly, optical-IR selected samples are subject to the effects of cluster and field galaxy evolution, which are, in general, also not well determined at  $z > 1$ . Note, however, that the evolution of the *elliptical* galaxy population in clusters has been shown by numerous authors (e.g., SED98 and references therein) to be remarkably simple and homogeneous. The apparent stability and smooth evolution of this dominant cluster population implies the selection functions for clusters defined by these galaxies can be computed with some confidence, even at  $z > 1$ . For a given cluster finding technique to be most useful, the reliable computation of selection functions is as critical as the sensitivity of the algorithm (Postman et al. 1996).

The general selection functions for clusters in most surveys are typically quite complicated functions of numerous parameters, including, but not limited to, the cluster redshift and the survey flux limits. However, in most cases, the detection rate for clusters of a given parameter set can generally be computed directly from the survey data, by inserting and attempting to recover fiducial test clusters. So long as the test clusters are a realistic representation of the cluster populations, this procedure will produce reliable results. False positive detections are however more difficult to quantify, as a thorough understanding of such false cluster detections requires some *a priori* knowledge of the contaminants – such as projection in optical catalogs (e.g., Postman et al. 1996) or contamination by active galactic nuclei in X-ray selected catalogs (e.g., Vikhlinin et al. 1998).

Indeed, the dominant cause of false-positive cluster candidates in optical cluster catalogs is projection. It has long been suggested that there are significant

projection effects in the Abell catalog (e.g., Lucey 1983), and even more modern cluster catalogs suffer significant false cluster detections due to random projections (Oke, Postman, & Lubin 1998; Holden et al. 1999). The projection-induced contamination in the Abell catalog has been studied with exhaustive n-body simulations, which show this to be primarily an artifact of the large aperture used to initially define the Abell catalog (van Haarlem, Frenk, & White 1997). These n-body results demonstrate that the false-positive rates due to projection for simulated cluster catalogs detected by either X-rays or 2-D galaxy overdensities is in fact quite similar, provided a similar detection aperture is used (van Haarlem, Frenk, & White 1997; also see López-Cruz & Yee 2000a, hereafter LCY00).

Given the extreme importance of galaxy clusters for a variety of studies, it is clear that large, well-understood samples of clusters are needed. In such a setting, it is desirable to have samples which are selected in as many ways as possible, at as many wavelengths as possible, as each sample will probe a somewhat different population with somewhat different selection effects. Furthermore, the cluster finding algorithms used should be as efficient as possible in terms of the required data, since clusters are rare objects and thus only found in large numbers in observationally expensive wide-field surveys. The method proposed below addresses these requirements. The method, which we term the Cluster-Red-Sequence (CRS) method, exploits the observational fact that the bulk of the early-type galaxies in all rich clusters lie along a linear color-magnitude relation. This relation, referred to hereafter as the red sequence, has been shown to have an extremely small scatter (e.g., Bower, Lucey, & Ellis 1992a,b) and appears to be extremely homogeneous from cluster to cluster (LCY00). In the CRS method, clusters are detected as over-densities in projected angular position, color and magnitude simultaneously. The color of the red sequence provides a precise redshift estimator for the detected clusters. The color constraint makes the CRS method extremely insensitive to projection effects, as random projections do not exhibit the necessary red sequence signature in the color-magnitude plane. This makes the CRS method fundamentally different from previous optical cluster finding algorithms. The concept of using the red sequence as a cluster marker, or to delineate cluster superstructures, has some history in the liter-

ature (e.g., Gladders & Yee 1998; Kaiser et al. 1998; Yee, Gladders, & López-Cruz 1999; Lubin et al. 2000; LCY00). However, this paper represents the first effort to cast the CRS method as a well-defined, well-motivated algorithm. The purpose is to describe an algorithm which is amenable to stringent testing, and useful for finding clusters in a wide range of optical-IR imaging data.

We have begun a large observational program, the Red-Sequence Cluster Survey (RCS), to identify and characterize clusters using the CRS method. This paper, the first of a series of two, describes the basic observational motivation for the CRS method, and provides a detailed algorithm and a test of that algorithm using existing data. The second paper in the series discusses the CRS as applied to the RCS data specifically, including a detailed derivation of the RCS selection functions for clusters, using extensive simulations.

This paper is arranged as follows. We describe and motivate the CRS method in the context of previous work and current observational constraints in §2 and §3. A detailed implementation of the method is given in §4. In §5 we provide a simple but powerful test of the method, using real redshift data from the CNOC2 Redshift Survey (Yee et al. 2000). Section 6 provides a brief discussion of possible refinements to the basic method outlined here. We summarize our findings in §7. A cosmology of  $H_0=70 \text{ km s}^{-1} \text{ Mpc}^{-1}$ ,  $\Omega_M=0.2$  and  $\Omega_\lambda=0.0$  is used throughout.

## 2. The CRS Method

By definition, optical/IR cluster-finding techniques all rely upon overdensities in galaxy distributions as the signature of mass overdensities. The basic premise shared by all such techniques is that galaxies are a reliable (though not necessarily unbiased, Kaiser 1984) tracer of the underlying mass distribution, which is the cosmologically interesting distribution. So long as the mass-to-light ratio of galaxy clusters is roughly constant, or evolving in well-understood ways, this basic premise seems sound. The most likely complication is the possible presence of dark clusters, though the current evidence indicates that such objects are rare at best (see §1 above). Given this basic premise, the differences between cluster finding-techniques are based in the manner in which each attempts to iden-

tify the real three-dimensional galaxy overdensities in typically two-dimensional imaging data. In general, the more modern techniques (the matched-filter technique, Postman et al. 1996; Kepner et al. 1999) are designed to be more sensitive to true clusters (while being less sensitive to random projections) at the expense of greater susceptibility to modeling uncertainties. The method we propose and test here makes the basic assumption that the presence of a red sequence of early-type galaxies is a ubiquitous and near-universal signature of clusters. This relatively strong assumption is well supported by the current observational evidence, and provides a very efficient and powerful method for detecting clusters. In the following we describe the basic advantages of this method and discuss some of the possible uncertainties, deferring a detailed description of the algorithm to §4.

The CRS method is motivated by the observation that all rich clusters have a population of early type galaxies which follow a strict color-magnitude relation. An example of this is provided in Figure 1, which shows the measured color-magnitude diagram for the  $z = 0.231$  cluster Abell 2390, from the HST data in Gladders et al. (1998). Current evidence (discussed in detail in §3) indicates that this galaxy population is remarkably homogeneous, both within individual clusters and between clusters. Moreover, it appears that the stellar population which makes up the red sequence is formed at high redshifts ( $z_f > 2$ ). In cold-dark-matter dominated scenarios of hierarchical structure formation this is the expected result, as present-day clusters are correlated with the most extreme initial overdensities, which are the first to collapse. Overall, cluster elliptical galaxies appear to have the oldest and most homogeneous stellar populations, and so can be expected to be a relatively stable marker of clustering.

There are numerous observational reasons which make the red sequence an attractive target for cluster finding, apart from its apparent homogeneity. First, elliptical galaxies generally dominate the bright end of the cluster luminosity function (e.g., Sandage, Bingelli, & Tamman 1985; Thompson 1986; Barger et al. 1998 – though see Rakos, Odell, & Schombert [1997] for an exception to this), and so are the most readily seen galaxies in a flux limited survey. Cluster elliptical galaxies are more luminous at higher redshifts (e.g., Schade, Barrientos, & Lopez-Cruz 1997; van

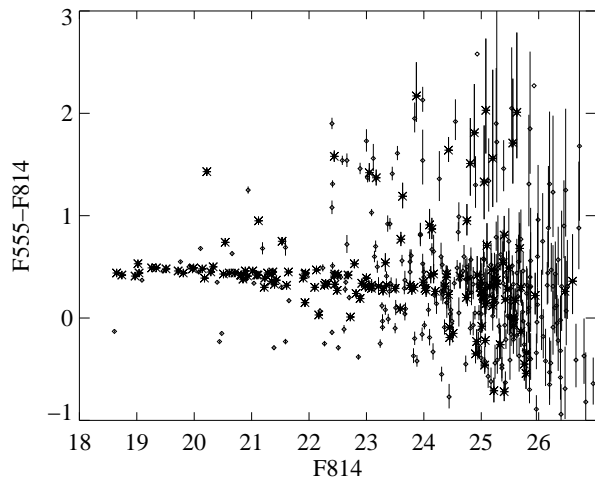


Fig. 1.— The observed color-magnitude diagram for Abell 2390, based on two-filter HST imaging of the cluster core. The data are from Gladders et al. (1998). The asterisks indicate galaxies morphologically selected as early-types, and diamonds indicate other galaxies in the image. Error bars are 1-sigma.

Dokkum et al. 1998), consistent with the age-induced fading expected in a passively evolving stellar population. In addition, the radial distribution of elliptical galaxies in regular, centrally concentrated clusters is more compact than that of other morphological types due to the morphology-density relation (Dressler et al. 1997 and references therein), and so presents a higher contrast against the background. Even in irregular clusters, with no well defined center, the morphology density relation holds, though at lesser significance (Dressler et al. 1997), and elliptical galaxies still trace the densest cluster regions. Additionally, elliptical galaxies have core-dominated compact brightness profiles, and so can be morphologically selected with a high level of confidence (Abraham et al. 1994; Gladders et al. 1998)

An examination of Figure 2 reveals the final, critical advantage of using elliptical galaxies to find clusters. Figure 2 shows model color-magnitude tracks, over a range of redshift, for galaxies of various spectral types (from Coleman, Wu, & Weedman 1980), as well as the expected location of the cluster red sequence, at similar  $z$ , using red sequence slopes from Kodama (1997). Since cluster elliptical galaxies likely represent the oldest stellar populations in the Universe, they are

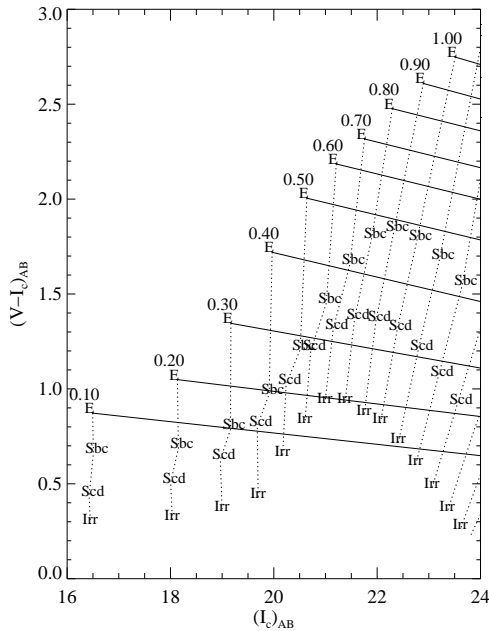


Fig. 2.— A simulated  $(V-I_c)_{AB}$  vs.  $(I_c)_{AB}$  color-magnitude diagram. Model apparent magnitudes and colors at various redshifts for several types of galaxies at a fixed  $M_I$  of -22. The dotted lines connect galaxies at the same redshift. Solid near-horizontal lines show the expected slope of the red sequence at each redshift.

as red or redder than any other galaxies at a given redshift. Moreover, with properly chosen filters straddling the  $4000\text{\AA}$  break, the cluster red sequence is as red or redder than other galaxies at a given redshift *and all lower redshifts*. As can be seen in Figure 2, this means that the bulk of the contaminant galaxies within a color slice corresponding to a red sequence at a given redshift are intrinsically bluer galaxies at yet higher redshifts. *In other words, the CRS method does not accumulate an overburden of foreground contamination when extended to higher redshifts, effectively solving the critical foreground projection problem with optical/IR cluster searches at such redshifts*. Moreover, projection effects due to background structures at higher redshift are minimized, because such structures will generally be most significant at yet redder colors.

A secondary advantage of using the red sequence as a cluster tracer is that the red sequence color provides

an extremely precise redshift indicator. LCY00 noted that the red sequence  $B - R$  (at a fixed apparent  $R$ ) versus redshift diagram for low  $z$  clusters shows a remarkably small scatter of  $\Delta z = 0.008$  about the mean relation. This had initially led López-Cruz (1997) to suggest that the red sequence color would be a valuable redshift indicator. Smail et al. (1998) came to similar conclusions, though with a much larger uncertainty, for their cluster sample at  $z \sim 0.25$ . SED98 found the red sequence color to be well correlated to redshift to  $z \sim 0.9$ . Notably, the redshift scatter implied by these simple photometric methods is comparable to the  $\Delta z = 0.02$  seen in four (or more) band photometric redshift studies with calibration redshifts (Brunner et al. 1997). This precision is a result of the significant reduction in photometric errors due to using many galaxies for a single color estimate, and the intrinsic similarity of red sequence galaxies.

In brief, the CRS method defines a cluster as an overdensity on the sky which also demonstrates an overdensity in the color-magnitude plane consistent with a red sequence of early-type galaxies. The method is remarkably insensitive to projection effects because the requisite color-magnitude relation is unlikely to be met by random projections. The enhanced sensitivity of the CRS algorithm to real clusters and its robust insensitivity to projections is a result of making the assumption that all significant real clusters have a red sequence of early-type galaxies. Though this assumption must break down at some point in the early formation of a cluster’s galaxies, it is observed to hold to at least  $z \sim 1.3$  in a variety of cluster environments and a range of cluster masses, as detailed below.

### 3. Observational Constraints on the Red Sequence as a Cluster Marker

Observations of the red sequence in clusters generally indicate that the bulk of the stars in the cluster early-type galaxies formed at a high redshift. Two major lines of evidence in support of this idea have been pursued by numerous authors. One is based on various analyses of the color evolution of the early-type galaxies. The other is based on analyses of the luminosity evolution of the early-type galaxies. Each general class of analysis is discussed separately below. Furthermore, since the observational data at  $z > 1$  are much less complete, the apparent properties of clus-

ters at these redshifts are discussed separately. All current data indicate that the red sequence is a universal signature of galaxy clusters.

### 3.1. Scatter, Color and Slope of the Red Sequence

Bower, Lucey, & Ellis (1992a,b) completed the first comprehensive photometric analysis of the red sequence properties in the Coma and Virgo clusters, and concluded that the early-type galaxies in each were indistinguishable. Considering that the Coma and Virgo clusters are prototypical clusters of completely different types – Coma is rich, massive, centrally concentrated, elliptical rich, and X-ray luminous; and Virgo is relatively poor, much less massive, irregular and spiral rich – this is a striking result. This basic result has been extended to a much larger sample in the exhaustive low-redshift cluster survey of LCY00. This multi-color imaging survey of 45 X-ray-selected Abell clusters provides a sample which encompasses a wide range of optical richnesses (Abell Richness Class 0 to  $> 2$ ), Bautz-Morgan classes (I-III), masses and Rood-Sastry classes (see López-Cruz & Yee 2000b for details of the sample). Despite this optical heterogeneity, every cluster in the sample has a red sequence; and the k-corrected slopes, scatters and colors of these red sequences are indistinguishable. At least at  $z < 0.2$ , the red sequence is a universal and homogeneous feature of galaxy clusters (LCY00).

Other surveys extend the conclusions of LCY00 to higher redshifts. Smail et al. (1998) studied 10 optically-selected luminous X-ray clusters at  $0.22 < z < 0.28$ , and Barrientos (1999) studied 8 optically-selected clusters at  $0.39 < z < 0.48$ . In each sample, the clusters have red sequences with colors and scatters which are remarkably homogeneous, and imply a high formation redshift. Notably, Barrientos (1999) suggests based on the  $z \sim 0.4$  data alone, that although cluster red sequence formation as low as  $z \sim 1$  is possible with appropriate arrangement of the cosmology, red sequence metallicity and star formation synchronicity, the most reasonable formation redshift from these data is  $z_f \geq 2.0$ . A similar result comes from Ellis et al. (1997) based on three clusters at  $z \sim 0.54$ .

The studies of Barrientos (1999), LCY00 and Smail et al. (1998) are the most comprehensive photometric studies of heterogeneous clusters samples over restricted redshift ranges. Most other surveys analyze clusters over a larger redshift range, up to redshifts of  $z \sim 1$ . Analyses of the evolution of the color (Aragón-Salamanca et al. 1993; Rakos & Schombert 1995; SED98; Kodama et al. 1998) all point to a high redshift of formation for the red sequence stellar populations. Complementary analyses of the scatter (SED98) and evolution of the slope (Gladders et al. 1998; SED98) over large redshift baselines indicate similar conclusions. The dominant uncertainty in much of this analysis is the implicit identification of the higher redshift clusters with lower redshift clusters of similar richness. As pointed out by Kauffmann (1995), in a hierarchical universe this identification is likely not correct, as the high redshift systems correspond to yet more massive clusters in the present day, and have a more vigorous merger history immediately prior to the epoch of observation when compared to present day clusters of similar mass. However, for our purposes, it is sufficient to recognize that the red sequences of the highest redshift clusters in these  $z < 1$  samples all satisfy the photometric properties of a high formation redshift.

A final line of evidence for the universality of the red sequence in clusters comes from the spectroscopic and photometric analysis of nine  $0.6 < z < 0.9$  optically selected cluster candidates by Oke, Postman, & Lubin (1998). Of the nine candidates, spectroscopic data indicate that six are real clusters. Of the six apparently real clusters, detailed information is available for three. The first, CL0023+0423, is in fact the projection of two sub- Abell Richness Class 0 groups (Lubin, Postman, & Oke 1998). CL0023+0423 shows a galaxy morphology mix similar to the field (Lubin et al. 1998), though 6 of the 24 spectroscopically confirmed members of both components of CL0023+0423 have the colors of cluster ellipticals at that redshift (Postman, Lubin, & Oke 1998). The second, CL1604+4304, is a massive, centrally concentrated cluster, and shows a strong, apparently old red sequence (SED98). The third, CL1324+3011, also shows a prominent red sequence (Gladders et al. 1998). Note that the well-formed clusters both show a red sequence, and even the projected groups show some evidence of red galaxies. In addition, another candidate, CL0231+0048, was initially included

in the sample precisely because it showed an anomalous lack of a red sequence (J.B. Oke, private comm.). Despite being a significant overdensity on the sky; spectroscopic analysis shows that it is not a real cluster (Oke et al. 1998). Furthermore, the fact that the Oke et al. sample includes cluster candidates which have a broad range of galaxy mixtures again argues against suggestions that optical cluster candidate catalogs such as these are biased to only clusters with old, well-developed galaxy populations. Rather, the optical samples available to date appear to sample a wide range of cluster types, and all true clusters in the samples appear to have a red sequence.

### 3.2. The Redshift Evolution of the Red Sequence Luminosity

The measured luminosity evolution of cluster early-type galaxies provides further evidence of the high formation redshift for the stars in these galaxies. Numerous fundamental-plane studies of clusters at redshifts up to 0.83 have demonstrated a change in the mass-to-light ratios of cluster galaxies consistent with that expected from passive evolution of stellar populations formed at high redshift (e.g., van Dokkum & Franx 1996; Kelson et al. 1997; Bender et al. 1998; van Dokkum et al. 1998; Jørgensen et al. 1999). Barrientos, Schade, & López-Cruz (1996), Schade et al. (1996) and Schade, Barrientos, & López-Cruz (1997) demonstrated similar evolution in the  $M_B - \log R_e$  relation (a projection of the fundamental plane); as did Pahre, Djorgovski, & de Carvalho (1996), Barger et al. (1998), and Ziegler et al. (1999) using the evolution of the Kormendy relation (Kormendy 1977). Further evidence for luminosity evolution comes from the evolution of the  $Mg_b - \sigma$  relation (e.g., Bender, Ziegler, & Bruzual 1996; Ziegler & Bender 1997). Taken together, these studies provide convincing evidence of the essentially passive evolution of the stellar populations in cluster ellipticals. Ziegler et al. (1999) do note that there are a number of possible uncertainties in such studies – however, the general conclusion that the bulk of the stellar population in these galaxies must have formed at  $z_f > 2$  still holds. As in the case of photometric color-based studies, it is difficult to provide more stringent limits, as this requires observations of clusters at higher redshifts than those explored so far.

### 3.3. The Red Sequence at $z > 1$

The universality of the red sequence is not yet well tested at  $z > 1$ , and analysis in the context of galaxy formation models is quite limited (e.g., SED98). This is simply due to a lack of candidate clusters at these redshifts, and the observational cost required to observe them. Despite this, optical and IR imaging of a portion of the limited sample of clusters does point to the universal presence of the red sequence. The highest redshift cluster discovered to date in a blank field imaging survey is CIG J0848+4453 at  $z = 1.273$  (Stanford et al. 1997). This cluster was first detected as a spatially compact overdensity of red galaxies in an optical-IR imaging survey – essentially as a detection of the red sequence. The radio galaxy 3C324 at  $z = 1.206$  is also embedded in a large cluster, which again shows a strong red sequence (Dickinson 1995). A further interesting case is the cluster AXJ2019+112 at  $z = 1.01$ . As discussed in §1, this cluster was first thought to be an optically dark cluster (Hattori et al. 1997), but was later revealed to be a normal cluster at  $z = 1.01$  with a strong red sequence (Benítez et al. 1999). da Costa et al. (1999) present color-magnitude diagrams for two  $z \sim 1$  cluster candidates detected in the ESO Imaging Survey (Olsen et al. 1999); both show a red sequence of early-type galaxies at the color appropriate to the estimated redshift, and are thus both likely real clusters. These candidates were selected on the basis of galaxy overdensities using the matched-filter technique. This technique makes no assumptions about galaxy colors and so the presence of a red sequence is not expected *a priori*. Notably, neither of these clusters is particularly rich (M. Franx, private comm.), which is expected given the total area from which the candidates were selected (1.1 deg<sup>2</sup>, Olsen et al. 1999).

It is striking that all the high-redshift clusters studied so far have red sequences. Except for CIG J0848+4453, the selection techniques for these clusters do not in general require such a signature – indeed, the cluster AXJ2019+112 was selected by a combination of X-ray emission and the lensing of a background quasar (Hattori et al. 1997) without any reference to cluster galaxies whatsoever. Moreover, the richness or mass range encompassed by these clusters is quite large (e.g., Smail & Dickinson 1995; Hattori et al. 1997; Stanford et al. 1997), with implied richnesses ranging from Abell Richness Classes 0 to

2, and most of the clusters being relatively poor. The implication is that the evolution of the cluster galaxy population towards a red sequence occurs at relatively small mass scales and thus prior to the assembly of large clusters. A recent weak-lensing analysis of MS1054–03 (a massive cluster at  $z = 0.83$ ) demonstrates this as well. MS1054–03 is clearly not relaxed, and appears to be composed of several sub-clumps with velocity dispersions (presuming an isothermal distribution) of  $\sigma_1 \sim 650 \text{ km s}^{-1}$  (Hoekstra, Franx, & Kuijken 1999a). Despite this, it already has a strong red sequence of early-type galaxies. Moreover, HST imaging and Keck spectroscopy of MS1054–03 reveals the presence of numerous galaxy-galaxy mergers, many of which are occurring between galaxies which are already red (Franx et al. 1999). Again, the implication is that the entrenchment of a red sequence in the cluster (i.e., the formation of the bulk of the stellar population in the eventual red sequence galaxies irrespective of the dynamical state of the host galaxies of said stars) occurs before the formation of the cluster as a massive relaxed system. In support of this general picture is the recent result of Ponman, Cannon, & Navarro (1999). On the basis of an analysis of the entropy of the X-ray gas in clusters and groups, Ponman et al. conclude that some form of pre-heating is required to explain the observed trends in X-ray temperature with cluster mass. Ponman et al. argue that this requires that the galaxies in clusters must form the bulk of their stellar populations prior to the assembly of the cluster, as is generally expected from hierarchical structure formation models.

Present observations thus indicate a paucity of mass overdensities (clusters, in the cosmological sense) which do not have a red sequence of early-type galaxies, even at  $z > 1$ . While it still remains possible that such clusters do exist, perhaps at some very early, low-mass stage of cluster assembly, it seems likely that they account for only a very small fraction of all clusters. Given this, it seems eminently reasonable to search for clusters using the red sequence.

#### 4. CRS Implementation

The implementation of the CRS method considers four main parameters for each detected galaxy in a survey: positions  $x$  and  $y$ , magnitude  $m$ , and color  $c$ . The color has an associated color uncertainty,  $\delta c$ ,

and the positions and magnitude are considered to be error-free. Photometric errors on the magnitude are ignored because the red sequence is nearly horizontal in a color-magnitude diagram (CMD). From the four input parameters for a set of observed galaxies, we wish to locate those positions which likely correspond to a galaxy cluster, and estimate a redshift,  $z$ . In summary, this is done as follows:

- 1) Define a series of overlapping color slices in the  $c$ - $m$  plane, guided by a fiducial red sequence model.
- 2) Select a subset of all galaxies as belonging to each slice, based on the probability (evaluated from  $m$ ,  $c$ ,  $\delta c$  and the model) that each galaxy belongs to that slice.
- 3) For a given subset, compute weights for all selected galaxies. The weight is based both on the galaxy magnitude, and the probability that each selected galaxy belongs to that slice.
- 4) Compute the weighted surface density of galaxy positions. All the slices taken together define a form of volume density in  $x$ ,  $y$  and redshift.
- 5) Identify the peaks in this volume and select clusters candidates using some significance cut.

The detailed implementation of this method is described in the following subsections.

##### 4.1. Color Slices

First, the expected photometric behavior of the red sequence as a function of redshift is determined from a default model of the red sequence. Defining the model essentially consists of selecting a cluster formation redshift,  $z_f$ . The details of the model are relatively unimportant, as any application to a real survey should include a verification of the model colors with spectroscopically confirmed cluster data. On the basis of this model, the color-magnitude diagram of the entire sample is divided into a number of regions bordered by the expected red sequence at various values of  $z$ . The choice of these bounding  $z$  values is driven by the data. Over the redshift range set by the filter combination, bounding red sequences are placed at

color separations,  $\Delta c$ , corresponding to:

$$\Delta c = (\delta c(c, m)^2 + \delta RS^2)^{\frac{1}{2}}, \quad (1)$$

where  $\delta c(c, m)$  is the measured color error of galaxies at a given color and magnitude. This fiducial color error is evaluated at values of  $c$  and  $m$  which correspond to a fixed absolute magnitude ( $M^*$  is used here) at various redshifts. Clearly, the color slices can be thought of as redshift slices, with a width in redshift,  $\Delta z$ , which is a function of  $\Delta c$  and the details of how color is mapped onto redshift. The second term,  $\delta RS$ , is the intrinsic scatter in color seen in cluster red sequences at moderate redshifts. A value of  $\delta RS = 0.075$  is used here (Barrientos 1999; SED98). Each “color slice” defined in this manner thus has a width sized relative to both the expected photometric scatter and the intrinsic scatter of the red sequence at the chosen redshift. In practice, the color slices are actually overlapped to ensure that no clusters are poorly sampled by being on the border between two slices. Figure 3 shows an example of the construction of color slices using data from the CNOC2 Redshift Survey patch CNOC0223+00 (Yee et al. 2000). The red-sequence model used in Figure 3 is described in detail in §5.

#### 4.2. Galaxy Subsets

For each color slice, defined by an upper and lower bounding red sequence, the probability that each galaxy in the sample belongs to that slice is then computed. This is done by assuming that the true colors are distributed normally about the measured colors, with Gaussian widths given by the measured color errors. The integration of each presumed error distribution in the desired color range then gives the probability that any given galaxy’s true color places it in the slice. A subset of galaxies based on a probability cut is then selected for each color slice. A probability cut of 10% has been used here. This value represents a compromise between sampling deeply in to the available data (as all faint galaxies have low probabilities of belonging to a given color slice because of large color errors) and computational efficiency (which improves with the smaller number of galaxies selected by a higher probability cut). An example of this probability assessment, using the same data and models as in Figure 3, is shown in Figure 4.

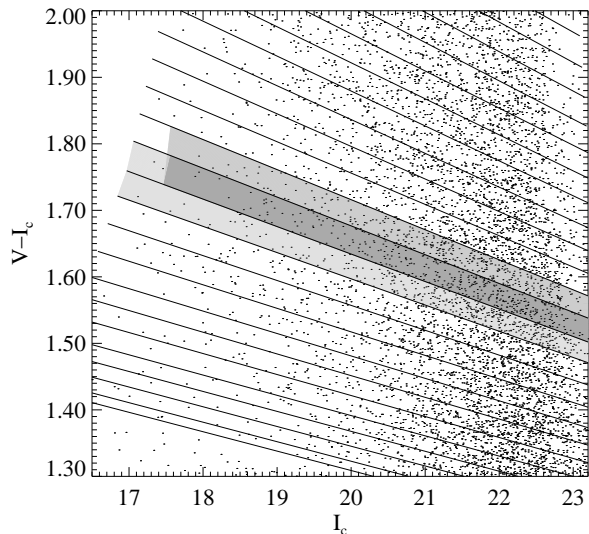


Fig. 3.— A portion of the observed  $V-I_c$  versus  $I_c$  CMD for the CNOC2 Redshift Survey patch CNOC0223+00. Bounding red sequences, constructed as detailed in the text, are shown as solid lines, from  $M^* - 1$  to the survey limits. Two overlapping color slices (shaded regions) are highlighted, with the overlap region a darker shade. For clarity, the shading in the second slice has been set 0.5 mags fainter than that in the first slice.

#### 4.3. Galaxy Weights

It is well known that field galaxy counts are in general steeper than the faint end of the typical cluster luminosity function (e.g., Lin et al. 1999; López-Cruz & Yee 2000b). Thus, at fainter magnitudes in a given color slice the field counts will eventually overwhelm the counts from any clusters. Without color selection, a similar effect happens toward brighter magnitudes, as the cluster counts are overwhelmed by counts from lower redshift galaxies. However, in any given color slice, because lower redshift galaxies are excluded by the color cut, any cluster elliptical galaxies likely dominate the bright end of a particular color slice, and so this effect is not expected at the bright end. This recognition that cluster galaxies of different magnitudes have a differing contrast against the background mandates the use of magnitude-based weighting of the galaxies, in addition to the weights taken directly from the color-based probability assessment discussed in §4.2.

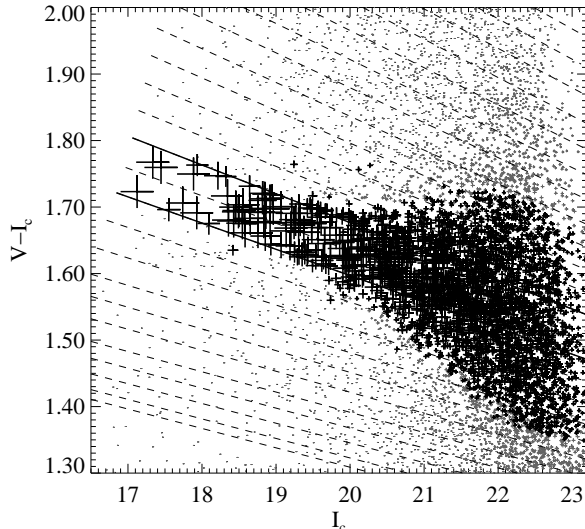


Fig. 4.— A CMD using the same data and models as Figure 3, but now showing the probabilities that each galaxy belongs to a particular color slice (the bluer of the two overlapping slices shown in Figure 3). The symbol size is proportional to the probability. Darker symbols indicate galaxies which pass the 10% cut discussed in the text.

The relative weight which should be assigned to a galaxy of a given magnitude can be deduced from the data, without reference to a model. This is done by computing the surface density of all objects in the color slice (with probability weights based only on the colors [§4.2], and using the density estimator described in §4.4 below). Galaxies located at the most significant peaks in the density are then designated as cluster galaxies (with field contamination) and the rest are designated as field galaxies. A comparison of these two samples of galaxies, after correcting for the field contamination in the cluster sample, then allows one to evaluate the probability that a galaxy of a given magnitude in the uncorrected cluster sample is in fact a cluster member. Put simply, if  $N_c(M)$  is the field-corrected, area-normalized counts for the cluster galaxies and  $N_f(M)$  is similarly for the field galaxies, then the probability that a galaxy of a given absolute magnitude  $M$  in the cluster sample is in fact a cluster member is:

$$P(M) = \frac{N_c(M)}{N_c(M) + N_f(M)}. \quad (2)$$

The construction of  $P(M)$  will depend on the available data. If each color slice contains enough data that a reliable  $P(M)$  can be computed, it is best to find  $P(M)$  on a slice-by-slice basis. This then allows for variations in the relationship between clusters and the field with color (i.e., redshift). However, in the data discussed in §5 (and illustrated in Figure 5) the survey area is not large enough, and so  $P(M)$  has been computed cumulatively over the entire color range considered. Furthermore, it is clear that for a particular cluster,  $P(M)$  is not absolute, as it will scale with the richness of that cluster. However, generally the variation in the ratio between values of  $P$  at different  $M$  is small, over a factor of a few in cluster richness counts. Furthermore, since the originally identified cluster galaxy sample is to first order representative of true clusters in the sample, this probability is adequate. An illustration of the computation of  $P(M)$ , using initial peaks with a range of significances (and hence richnesses), is shown in Figure 5. It shows the run of  $P(M)$  with magnitude for the data discussed in §5, using two different significance cuts to identify initial peaks, and hence the “cluster” subsample. The size of the two different “cluster” subsamples differ by an order of magnitude, in that they represent 2% and 20% of all galaxies in the sample, and yet the difference between the relative values of  $P(M)$ , expressed by the slope of linear fits to the  $P(M)$  vs.  $M$  relation, is only a factor of 1.5. Based on this, we use a cut of 10% in the computations presented in §5, as this adequately spans the extreme values illustrated in Figure 5.

An additional modification is made to  $P(M)$ , in which  $P(M)$  for all galaxies brighter than the expected cluster  $M^*$  is set equal to  $P(M^*)$ . This correction is based on the observation that without such a modification, an unacceptable level of stochastic noise is introduced from the few bright galaxies in a given slice. With a final  $P(M)$  computed, a weight,  $w$ , is then assigned to each galaxy in a given subset. The assigned weight is simply the product of the probability of being included in the color-slice subset (subject to some lower threshold as detailed in §4.2) and  $P(M)$ .

#### 4.4. The Galaxy Surface Density

With a list of positions,  $x$  and  $y$ , and associated weights,  $w$ , now in hand, the next step is to evaluate the surface density of objects. We have considered

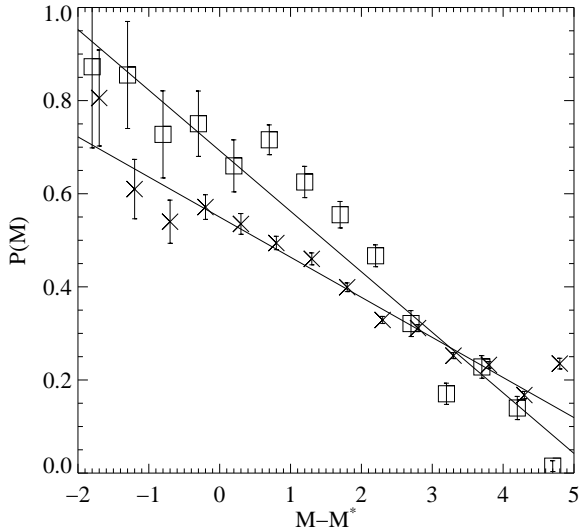


Fig. 5.— Values of  $P(M)$  versus  $M$  computed for the data discussed in §5. Cuts representing 2% (squares) and 20% (crosses) of all galaxies in the sample are shown. Solid lines give the best fit line for each subsample.

a number of estimators for this, and have settled on simple fixed-kernel smoothing. We considered in detail the more complicated adaptive kernel smoothing used by Gal et al. (2000), but have decided that this estimator is actually inappropriate for this particular application. Fundamentally, the tendency of the adaptive kernel to break up regions of high density (i.e., clusters in the data) into smaller features is not desirable. Estimators such as the adaptive kernel are motivated on purely mathematical grounds (Vio et al. 1994) and may not be appropriate to a given physical situation, as is the case here.

The fixed-kernel estimator is used to produce a surface density map of the galaxies in the color slice. This map is simply the weighted convolution of the kernel with the data points at positions  $x, y$ , evaluated over a grid spanning the range of the data (see Vio et al. for details). Hereafter, the value of the kernel-smoothed density at a particular location  $i, j$  in the map is referred to as  $\delta_{ij}$ . Two different forms were considered for the smoothing kernel:  $k(r) \propto e^{Cr}$  and  $k(r) \propto e^{Cr^{1/2}}$ . When appropriately scaled, both give profiles akin to several standard forms used to describe cluster radial density profiles. However, ex-

periments on data from the CNOC2 project (see §5) showed the former kernel to be better suited, as the cuspy core of the latter kernel tends to produce density maps with spurious strong peaks associated with individual bright (and hence large weight) galaxies which lie at the kernel cusp. The final form of the kernel used is:

$$k(r) = Ae^{(-1.965r)}, \quad (3)$$

where  $r$  is the proper distance from the kernel center. In this normalization, the radius  $r$  is expressed in units of the scale radius of the more familiar Navarro, Frenk, & White (1997) (NFW) profile. The exponential constant of  $-1.965$  is derived by requiring that the adopted profile fit the NFW profile at intermediate radii, and is constant provided that  $r$  is expressed in units of the NFW scale radius. The relation between the two profiles considered and several other standard forms for cluster density profiles is given in Figure 6. The various data for the standard profiles are taken from Adami et al. (1998). Also, in Equation 3,  $A$  is a normalizing factor chosen so that:

$$\int_0^{r_{max}} k(r) dr = 1. \quad (4)$$

A scale radius of  $0.33 h^{-1}$  Mpc has been used for the tests described in §5 below, a value suggested by measurements of the CNOC1 cluster sample (Carlberg et al. 1996, 1997b). The maximum radius,  $r_{max}$ , is taken as four times the scale radius. It should be noted that the inability of other authors to strongly distinguish between possible profile shapes (e.g., King, Hubble or NFW [Adami et al. 1998]; Hernquist or NFW [Carlberg, Yee, & Ellingson 1997]) even with large cluster samples indicates that the exact shape of the kernel is not of overwhelming significance. Lubin & Postman (1996) similarly found that the precise shape of the radial filter in the PDCS had little effect on the detectability of clusters in that survey.

Prior to the merging of the individual 2D density maps into a data cube, the  $\delta_{ij}$ s must be transformed to some standard measure (such as  $\sigma$  of detection). This is necessary because the meaning of a given density value changes between the slices (both because of the apparent change in the size of the fixed-metric kernel, and because of the change in the mean density of objects relative to the kernel size). As in Gal et al.

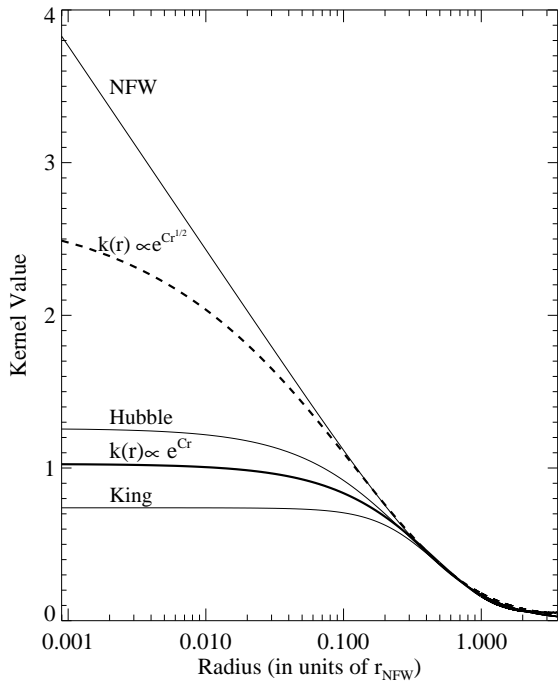


Fig. 6.— Various possible density-estimation kernels. Three standard cluster profiles (NFW, King, and Hubble) as well as the two kernels discussed in the text, are shown at radii from 0.001 to 4.0 times the NFW core radius.

(2000), the bootstrap technique is used to evaluate the significance of peaks relative to the background distribution. However, it is worth noting that a simple application of the bootstrap technique is likely not correct, as one of the fundamental underpinnings of the bootstrap process is the assumption that the data points to be analyzed are independently and identically distributed (Press et al. 1992). In data presumed to contain clusters this is clearly not true. However, as the clusters occupy only a small fraction of the total surface area of any map, it is possible to exclude some fraction of the highest valued regions (and lowest, to preserve symmetry) of the map. The same regions in the bootstrap realization maps of the data (acquired by sampling the data with replacement and re-running the kernel smoothing) are excluded in turn. The probability distribution function (PDF) for density values in the remaining areas of the bootstrap maps then closely matches the background distribution of the initial map. Experimentation shows that an exclusion cut of only the 10% highest and lowest density values is enough to solve this problem. Figure

7 illustrates the result of this process, using the density map from a single color slice of the data discussed in §5. Several derived background distributions of  $\delta_{ij}$  are shown. The first, and best fitting distribution is based on the bootstrap method. For comparison, another distribution, constructed by replacing the correlated galaxy positions with random positions (but keeping the same weights as the real data) is also shown. Obviously, the restricted bootstrap dataset provides a good representation of the background distribution found in the input data, while the dataset based on random positions does not.

The probability of a given value of  $\delta_{ij}$  occurring at random can then be evaluated from the restricted bootstrap dataset. This is best done by a direct analysis of the bootstrap PDF as it is often non-normal. Each value of  $\delta_{ij}$  in the input map is transformed into a probability,  $P(\delta_{ij})$ , by evaluating the likelihood that a value of  $\delta_{ij}$  or greater occurs in the the restricted bootstrap dataset. In other words:

$$P(\delta_{ij}) = \frac{N(\delta_{bootstrap} \geq \delta_{ij})}{N(\delta_{bootstrap})}. \quad (5)$$

The raw probabilities can then be transformed to more familiar Gaussian sigmas if desired, though such a change is essentially cosmetic.

#### 4.5. Identifying and Characterizing Clusters

Once probability maps have been constructed for each slice, the slices can be stacked together to form a data-cube. The generation of a cluster catalog from this data-cube is then simply a matter of selecting high probability regions, subject to some predetermined probability cut. The details of how to do this optimally will not be described here, as the process is data dependent, though not complicated. A further exploration of this topic, in the context of a particular survey and detailed simulated data, can be found in paper II ( Gladders & Yee 2000b), or in §5 below. It should be noted that other authors have used relatively simple algorithms in this final step with good success (Postman et al. 1996); similar simple algorithms should work as well.

With a cluster candidate identified, the final step is to estimate a redshift for each candidate. This is done directly from the above data-cube, as the redshift of a given cluster candidate is encoded by the location of

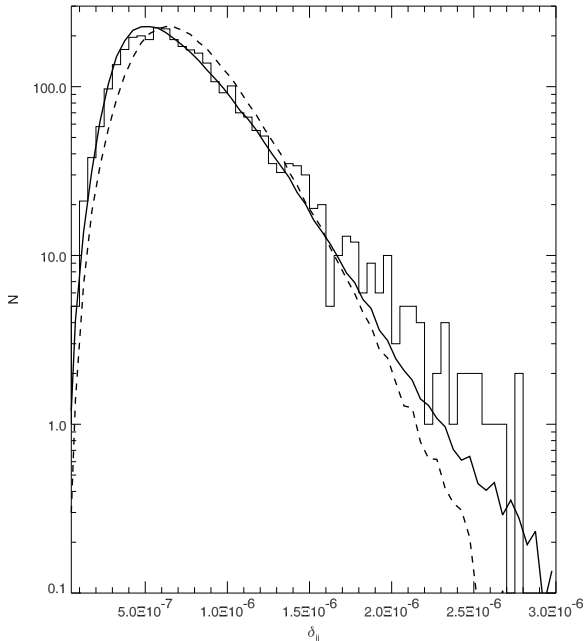


Fig. 7.— The histogram illustrates the actual distribution of  $\delta_{ij}$ s from a single color slice of the dataset discussed in §5. The background distribution as deduced from the bootstrap approach discussed in the text is shown as a thick solid line. Another background distribution, based on random positions is shown as a dashed line. The excess of high-valued points is the signature of several significant peaks in the density map for this particular color slice.

the peak along a line passing through the color axis of the stacked density maps at the  $x$ - $y$  position of the candidate.

## 5. A Test of the CRS Method

The CNOC2 dataset (Yee et al. 2000) provides an useful testbed for cluster-finding algorithms, and has kindly been provided in advance of publication by the rest of the CNOC2 group. This intermediate redshift field galaxy survey consists of 4 patches of data. Each patch is  $\sim 0.39 \text{ deg}^2$  in size. The surveys consists of  $UBVR_cI_c$  imaging and spectroscopy for a large sample of galaxies ( $\sim 40,000$  in the photometric catalog to the 100% completeness limit of  $R=23$ , with  $\sim 6000$  spectroscopic redshifts for galaxies typically as faint as  $R=21.5$ ). However, the layout of each patch is complex, as the patches were designed to sample the

correlation function, rather than to minimize patch edges, and so are not optimal for cluster detections. Additionally, the CNOC2 redshift catalog is sparsely sampled, and is somewhat biased against detecting compact structures (due to the unavoidable exclusion of an above average number of galaxies in dense regions when using a multi-object spectrograph – see Yee et al. 2000 for details). Nevertheless, the availability of a large spectroscopic sample outweighs any such considerations, and makes the CNOC2 survey an indispensable aid in assessing the suitability of the CRS method. Note that in considering the output of the photometric cluster-finding process, it is necessary to make some analysis of the CNOC2 redshift sample in order to identify real bound structures in the redshift data. This process is complex, particularly because of the sparseness of the redshift sampling, and the complex weighting functions incurred by the use of a multi-object spectrograph. A global and rigorous analysis of bound structures in the CNOC2 redshift survey data will be presented by the CNOC2 group (Carlberg et al. 2000). This paper uses a simplified process, described below, to provide a first-pass comparison with the CRS method.

To test the CRS method, a dataset was constructed over the entire CNOC2 survey area using a subset of the available photometry. Only fields in which  $I_c$  magnitudes,  $V - I_c$  colors,  $\Delta(V - I_c)$  color errors, and  $x$  and  $y$  positions are available were used, and these provide the input to the CRS algorithm. The total area covered by this subset is 1.48 square degrees. Over the CNOC2 spectroscopically unbiased redshift range ( $0.12 < z < 0.55$ ), this area corresponds to a volume of  $2.7 \times 10^5 h^{-3} \text{ Mpc}^3$ . Note that rich clusters occur with a density of about 1 every  $10^5 - 10^6 h^{-3} \text{ Mpc}^3$  (Bahcall 1999), so we expect to find only poor clusters and groups in this volume. The CRS algorithm was then run across all four patches, with the redshift range restricted to  $0.1 < z < 0.6$  (somewhat larger than the redshift range over which spectroscopic confirmation of the clusters can be expected). The red-sequence model used is based on a 0.5 Gyr burst (drawn from the GISSEL library, Bruzual & Charlot 1993) completed at  $z=3$ , evolving to lower redshifts with a metallicity-luminosity relationship which reproduces the red-sequence slope in the Coma cluster at  $z \sim 0$  (Gladders et al. 1998). A portion of the results of the CRS cluster-finding is shown in Figure 8 for the CNOC0223+00 patch. A

number of significant sources are obviously detected. In these data, values of  $\delta_{ij}$  have been re-cast in Gaussian sigmas, referred to hereafter as  $\sigma_{ij}$ .

Individual sources were then selected from the data-cubes using the clump finding algorithm of Williams, de Geus, & Blitz (1994). This algorithm was originally developed for locating structure in position-position-velocity radio data. Williams et al. discuss the accuracy of their clump finding technique in detail; in summary, it works by contouring the data in 3-D at multiple levels, and following clumps through the various levels from an initial peak value, identify sub-clumps as appropriate. Because the algorithm assumes no clump profile, it is readily applied to the CRS position-position-redshift data-cubes. Via extensive simulations, Williams et al. recommend that the data be contoured at levels which are separated by  $\Delta T=2T_{RMS}$ . In the original application,  $T_{RMS}$  is the root-mean-square error in the temperature of the position-position-velocity data. A similar statistic can be estimated from the CRS data-cubes by examining random realizations of the position and weight data used to construct the data-cubes. These random realizations, which are distinct from the bootstrap realizations discussed in §4.4, have the same weights as the original input data but randomized positions, and are used within the algorithm primarily to account for irregular patch edges. In the particular CNOC2 data discussed here, the RMS of the random realizations is about  $\Delta\sigma_{ij}=0.55$ . The RMS is not directly indicated by the distribution of  $\sigma_{ij}$ s in the real data-cube as a whole (i.e. the bootstrap normalized data-cube, cast in  $\sigma_{ij}$ s, does *not* have a noise of  $\Delta\sigma_{ij}=1$ ), as this represents a scaling relative to the distribution of the data as a whole, including all real structures. Hence, for the data discussed here, the Williams et al. clump-finder was run using  $\Delta\sigma=1.1$ , down to a contour level of  $\sigma_{ij} = 2.4$ . This means that the lowest significance peaks detected have a maximum significance of  $3.5\sigma$  (1 contour above the lowest contour level) and all detected peaks, regardless of maximum significance, are traced to  $2.4\sigma$ .

For each selected clump in the data-cube, a redshift was estimated from the position of the clump maximum projected along the  $z$ -axis of the data-cube. All CNOC2 galaxies with spectroscopic redshifts within a projected distance of  $0.5 h^{-1}$  Mpc of the projected clump in  $x$  and  $y$  were then selected.

A simple friends-of-friends analysis of these galaxies (compared to the entire redshift sample) was then performed. A fixed linking length of  $0.5 h^{-1}$  Mpc in angular space, and  $400 \text{ km s}^{-1}$  in redshift space was used throughout. This simple analysis serves to identify likely associated objects in the redshift sample. A visual examination of the redshift distribution of the selected subset of galaxies, taking into account both the distance from the clump center and the number of friends each galaxy has is then used to select (if possible) a structure corresponding to the identified clump. In cases where more than one structure appears in the redshift subsample, the structure closest to the  $x$ - $y$  position is used. In such cases, there are often other identified clumps which appear associated with the other structures, but untangling the correspondence between various clumps and redshift structures is straightforward. Figure 9 shows three examples of this process using data from a portion of the central block of the patch CNOC0223+00 (the right hand portion of the  $\sigma_{ij}$  maps shown in Figure 8). There are three significant peaks in this region, all in the redshift interval  $0.35 < z < 0.45$ . Each is readily associated with a different redshift structure, despite the close proximity of the peaks both in redshift and angle. The first two of these example redshift structures are particularly close – separated by only  $1700 \text{ km s}^{-1}$  in redshift, and  $0.9 h^{-1}$  Mpc projected on the sky – yet each is clearly identified as a separate redshift structure, and as a separate CRS peak.

Figure 10 presents the comparison of the CRS algorithm output to the CNOC2 redshift sample. CRS cluster candidates both with and without a redshift counterpart are shown. CRS cluster candidates with peak significance in either the first or last color slice, indicating that the predicted redshift may be in error, are flagged. This possible error is small at the lower redshift end (where the color errors are small and hence color slices are narrow in redshift) but could be quite significant at the upper redshift end. The photometric redshifts have been adjusted by a quadratic fit to an initial comparison between the spectroscopic and raw photometric redshifts in order to account for any uncertainties in the early-type galaxy spectral energy distribution model. As mentioned §4.1, any real cluster survey is likely to include the training data necessary for this calibration process. Several points of note are apparent from Figure 10.

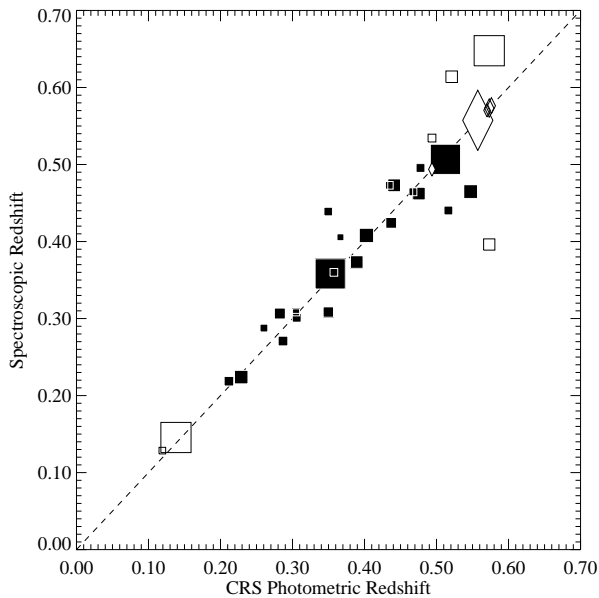


Fig. 10.— The comparison between the CRS photometric redshifts (from the  $I_c - V$  red sequence) and CNOC2 spectroscopic redshifts. Squares are CRS cluster candidates which have a redshift counterpart; diamonds are those which do not. Open symbols represent objects in which the peak significance is in either the first or last color slice (i.e., at the edges of the nominal redshift range of the CNOC2 survey).

First, considering the subsample at  $z < 0.5$ , the false-positive rate is very low, with only 1 of 23 candidates not detected in the spectroscopic sample, and even that one is at a relatively high  $z$  of 0.49. At  $z > 0.5$ , the apparent false-positive rate is much higher, with 4 of 11 candidates not showing any spectroscopic counterparts. This is likely a result of incompleteness in the redshift sample. As the CNOC2 redshift data is sparsely sampled, very poor cluster/group systems (with only a few bright galaxies in total), or systems in the higher redshift range (with only a few bright galaxies in the spectroscopic sample) may not be well represented.

Second, the redshift accuracy of the method is extremely good, bearing out suggestions made in previous work (LCY00; Smail et al. 1998). The standard deviation of the difference between the color-estimated redshifts and the spectroscopic redshifts at  $z < 0.5$  is only  $\Delta z = 0.026$ . The apparent redshift

scatter at  $z > 0.5$  is much higher, with one nominally confirmed candidate with a redshift error of 0.18. This particular candidate is found only in the highest redshift slice (as are most unidentified candidates), and this large redshift error may thus be due to a misidentification of a system at a real redshift beyond the spectroscopic reach of CNOC2 which has been falsely identified with a lower redshift system which is along a similar line of sight and is too poor to have been found by the CRS method as applied here.

Regardless, the results at  $z < 0.5$  clearly indicate that the CRS method is very successful in identifying real overdensities, and that the redshift estimates are extremely accurate. There are three reasons for the ability of the CRS method to obtain such high accuracy using only two filters: 1) the use of a known and empirically calibrated spectral energy distribution, 2) the fact that E/S0 galaxies have the strongest spectral breaks and hence provide a strong color signature with redshift, and 3) the estimation of the redshift for any given cluster by using colors for a number of individual galaxies simultaneously.

Finally, it should be recalled that the volume probed by the survey considered here is quite small (in cluster terms) and that it is expected that most of the systems identified above should be quite poor. This expectation is well borne out by a weak-lensing examination of several CNOC2 fields (Hoekstra, Franx & Kuijken 1999b) and a preliminary dynamical analysis of the groups in the CNOC2 survey (R. Carlberg, private comm.). These independent analyses indicate that most of the systems have 1-D velocity dispersions of only 200-400  $\text{km s}^{-1}$ , well below the lower end of Abell Richness Class 0 ( $\sim 650 \text{ km s}^{-1}$ , Yee et al. 2000b), and generally much poorer than systems identified using previous cluster finding algorithms. Though it is almost certain that the CRS results shown here do not represent a 100% complete sample at such masses, the success in finding *any* such low-mass systems at these intermediate redshifts using only 2-color photometry is a strong validation of the general method. In addition, the extremely low ( $< 5\%$ ) false positive rate compares very favorably to the generally higher contamination in optical cluster catalogs constructed by other means (e.g., Oke et al. 1998). Furthermore, the upper limit of redshift explored here was selected to reflect the spectroscopic

limits of the CNOC2 survey; there is no reason why the CRS method cannot be applied at yet higher redshifts. Limiting the required wide-field data to that from CCDs, a reasonable upper limit is about  $z \sim 1.4$  – corresponding to having the 4000Å break at the red end of typical CCD sensitivities.

## 6. Possible Algorithm Refinements

A number of refinements or modifications of the general method described above are possible. For example, given enough information to construct appropriate field and cluster models, one could replace the slicing, smoothing and stacking approach used above by a maximum-likelihood based approach (Postman et al. 1996; Kepner et al. 1999). Such models can likely be deduced internally from a large enough cluster-search dataset. Additionally, entirely different density estimators could be used. For example, the Voronoi tessellation approach of Kim et al. (1999) is likely applicable with only minor modification of the general algorithm described above. Many of the approaches used in X-ray astronomy to detect diffuse collections of points embedded in a background (e.g., Campana et al. 1999, and references therein) are applicable here, with the galaxies treated analogously to single photons. The purpose of this paper is not to lay out the definitive algorithm for using the red sequence to locate clusters. Rather, the intention has been to describe a particular, and well-motivated algorithm which can be used to demonstrate the effectiveness of the basic premise of the CRS method applied to real data.

One major modification of the basic method outlined here would be the addition of morphological information. It is possible, even with ground based imaging, to deduce the likely morphological classification of a galaxy using simple and computationally tractable estimators (e.g., Abraham et al. 1994). Specifically, one can assign a probability of being an early-type galaxy to all galaxies in a survey. Including such analysis into the algorithm described above would be relatively simple, as this probability can be incorporated into the weights assigned to each galaxy. However, constructing the morphological probability assessment of a given galaxy in real imaging data is a significant task, as this assessment is a function of numerous factors (i.e., the seeing, the sampling, the depth of the imaging relative to the galaxy magni-

tude, the galaxy redshift and intrinsic size etc.). Furthermore, in the CNOC2 data discussed above, the imaging is also affected by serious camera distortions. We have thus not attempted to incorporate morphological data into the above analysis. However, given the basic premise of the CRS method, it is obvious that morphological filtering will be of benefit.

## 7. Conclusions

Numerous large studies to  $z \sim 1$  have now demonstrated that the red sequence of early-type galaxies is a universal and homogeneous feature of galaxy clusters. Based on this strong observational fact, we have developed a new technique, the CRS method, for locating clusters in 2-filter optical or infrared imaging data. Using appropriate filters, the CRS method circumvents problems with foreground, and to some extent background, projection effects which have been so problematic in previous optical cluster surveys. A specific algorithm has been constructed to implement this general method. This algorithm constructs 2-D smoothed density maps of color slices corresponding to redshifts bin, which are then normalized and re-assembled into a 3-D density data-cube. Peaks in this data-cube are then defined as cluster candidates. Using data from the CNOC2 survey we have tested the CRS method over a significant redshift range. From this test, and the general data on the evolution of cluster early-type galaxies available in the literature, we conclude the following:

- 1) The apparent universality of the red sequence in available data, even to redshifts greater than one, indicates that the CRS method should be applicable to the entire redshift range accessible to CCDs ( $0 < z < 1.4$ ).
- 2) The CRS method is a powerful new approach to finding galaxy clusters in imaging data at optical and infrared wavelengths. The performance of the method shows that it is able to reliably detect rather poor bound structures ( $\sigma_v \leq 400$  km s<sup>-1</sup>) with a very low contamination rate of less than 5%, using data of only moderate depth.
- 3) The redshift accuracy of the method is  $\Delta z \sim 0.025$  over the redshift range  $0.1 < z < 0.5$ , or equivalently 10% in redshift. This accuracy is comparable to that

achieved for single galaxies using four (or more) filter photometric redshift methods.

We have begun a large survey, the RCS, designed to exploit the power of the CRS method (e.g., Gladders & Yee 2000a). The primary survey data are 100 square degrees of imaging in two filters ( $R_c$  and  $z'$ ), to the depth necessary to find clusters to  $z \sim 1.4$ . Paper II of this series (Gladders & Yee 2000b) discusses the application of the CRS method to the RCS data specifically, and further explores the applicability and completeness of the method to redshifts as high as  $z \sim 1.4$ . Unlike this paper, the main results of paper II are based on a broad and comprehensive set of tests performed on simulated data, created using detailed and realistic galaxy and cluster models.

M.D.G. thanks the Natural Sciences and Engineering Research Council (NSERC) of Canada for support via PGSA and PGSB graduate scholarships. H.K.C.Y. thanks NSERC for support via an operating grant. M.D.G. thanks Ray Carlberg for numerous useful discussion on statistics and the bootstrap method. We are particularly indebted to the CNOC2 group for providing access to the CNOC2 dataset in advance of publication.

## REFERENCES

- Abraham, R.G., Valdes, F., Yee, H.K.C., & van den Bergh, S. 1994, *ApJ*, 432, 75
- Adami, C., Mazure, A., Katgert, P., & Biviano, A. 1998, *A&A*, 336, 63
- Aragón-Salamanca, A., Ellis, R.S., Couch, W.J., & Carter, D. 1993, *MNRAS*, 262, 764
- Bahcall, N.A. 1999, *Formation of Structure in the Universe*, eds. A. Dekel & J.P. Ostriker, Cambridge, Cambridge University Press, 135
- Bahcall, N.A. & Fan, X. 1998, *ApJ*, 504, 1
- Barger, A.J., Aragón-Salamanca, A., Smail, I., Ellis, R.S., Couch, W.J., Dressler, A., Oemler, A., Poggianti, B.M., & Sharples, R.M. 1998, *ApJ*, 501, 522
- Barrientos, F., Schade, D., & López-Cruz, O. 1996, *ApJ*, 460, 89
- Barrientos, L.F., 1999, Ph.D. Thesis, University of Toronto
- Bender, R., Saglia, R.P., Ziegler, B., Belloni, P., Greggio, L., Hopp, U., & Bruzual, G. 1998, *ApJ*, 493, 529
- Bender, R., Zeigler, B., & Bruzual, G. 1996, *ApJ*, 463, 51L
- Benítez, N., Broadhurst, T., Rosati, P., Courbin, F., Squires, G., Lidman, C., & Magain, P. 1999, *ApJ*, 527, 31
- Bower, R.G., Bohringer, H., Briel, U.G., Ellis, R.S., Castander, F.J., & Couch, W.J. 1994, *MNRAS*, 263, 345
- Bower, R., Lucey, J.R., & Ellis, R.S. 1992a, *MNRAS*, 254, 589
- Bower, R., Lucey, J.R., & Ellis, R.S. 1992b, *MNRAS*, 254, 601
- Brunner, R.J., Connolly, A.J., Szalay, A.S., & Bershad, M.A. 1997, *ApJ*, 428, 21L
- Bruzual, G. & Charlot, S. 1993, *ApJ*, 378, 47
- Campana, S., Lazzati, D., Panzera, M.R., & Tagliaferri, G. 1999, *ApJ*, 524, 423
- Carlberg, R.G. et al. 2000, in preparation
- Carlberg, R.G., Yee, H.K.C., & Ellingson, E. 1997, *ApJ*, 478, 462
- Carlberg, R.G., Yee, H.K.C., Ellingson, E., Abraham, R.G., Gravel, P., Morris, S.L., & Pritchet, C.J. 1996, *ApJ*, 462, 32
- Carlberg, R.G., Morris, S.L., Yee, H.K.C., & Ellingson, E. 1997a, *ApJ*, 479, 19L
- Carlberg, R.G., Yee, H.K.C., Ellingson, E., Morris, S.L., Abraham, R.G., Gravel, P., Pritchet, C.J., Smecker-Hane, T., Hartwick, F.D.A., Hesser, J.E., Hutchings, J.B., & Oke, J.B. 1997b, *ApJ*, 485, L13
- Castander, F.J., Ellis, R.S., Frenk, C.S., Dressler, A., & Gunn, J.E. 1994, *ApJ*, 424, L79
- Clowe, D., Luppino, G.A., Kaiser, N., Henry, J.P., & Gioia, I.M. 1998, *ApJ*, 497, 61L
- Coleman, G.D., Wu, C.-C., & Weedman, D.W. 1980, *ApJS*, 43, 393
- da Costa, L., Scodreggio, M., Olsen, L.F., Nonino, M., Rengelink, R., Bender, R., Franx, M., Jorgensen, H.E., Renzini, A., & Rosati, P. 1999, *A&A*, 343, L29
- Dickinson, M. 1995, in *ASP Conf. Proc. 86, Fresh Views on Elliptical Galaxies*, eds. A. Buzzoni et al. (San Francisco: ASP), 283
- Dressler, A., Oemler, A., Couch, W.J., Smail, I., Ellis, R.S., Barger, A., Butcher, H., Poggianti, B.M., & Sharples, R.M. 1997, *ApJ*, 490, 577
- Ellis, R.S., Smail, I., Dressler, A., Couch, W.J., Oemler, A., Butcher, H., & Sharples, R.M. 1997, *ApJ*, 483, 582
- Fan, X., Bahcall, N.A., & Cen, R. 1997, *ApJ*, 490, 123L
- Franx, M., van Dokkum, P.G., Fabricant, D.G., Kelson, D., & Illingworth, G.D. 1999, *ApJ*, 520, L95
- Gal, R.R., de Carvalho, R.R., Odewahn, S.C., Djorgovski, S.G., & Margoniner, V.E. 2000, *AJ*, 119, 12
- Gioia, I.M. & Luppino, G.A. 1994, *ApJS*, 94, 583
- Gladders, M.D., López-Cruz, O., Yee, H.K.C., & Kodama, T. 1998, *ApJ*, 501, 571
- Gladders, M.D., & Yee, H.K.C. 1998, in *Proceedings of the CFHT User's Meeting*, eds. P. Martin & S. Rucinski, (Hawai'i: CFHT)
- Gladders, M.D., & Yee, H.K.C. 2000a, in *ASP Conf. Proc. Cosmic Evolution and Galaxy Formation: Structure, Interactions and Feedback*, eds. J. Franco et al. (San Francisco: ASP), in press (astro-ph/0002340)
- Gladders, M.D., & Yee, H.K.C. 2000b, in preparation (paper II)
- Gramann, M., Bahcall, N., Cen, R., & Gott, R.J. 1995, *ApJ*, 441, 449

- Hattori, M., Ikebe, Y., Asaoka, I., Takeshima, T., Boehringer, H., Mihara, T., Neumann, D.M., Schindler, S., Tsuru, T., & Tamura, T. 1997, *Nature*, 388, 146
- Hoekstra, H., Franx, M., & Kuijken, K. 1999a, preprint (astro-ph/9910487)
- Hoekstra, H., Franx, M., & Kuijken, K. 1999b, preprint (astro-ph/9911106)
- Holden, B.P., Nichol, R.C., Romer, A.K., Metevier, A., Postman, M., Ulmer, M.P., & Lubin, L.M. 1999, *AJ*, 118, 2002
- Jørgensen, I., Franx, M., Hjorth, J., & van Dokkum, P.G. 1999, *MNRAS*, 308, 833
- Kaiser, N. 1984, *ApJ*, 248, L9
- Kaiser, N. 1995, *ApJ*, 439, L1
- Kaiser, N., Wilson, G.W., Luppino, G., Kofman, L., Gioia, I., Metzger, M., & Dahle, H. 1998, preprint (astro-ph/9809268)
- Kauffmann, G. 1995, *MNRAS*, 274, 153
- Kelson, D.D., van Dokkum, P.G., Franx, M., Illingworth, G.D., & Fabricant, D. 1997, *ApJ*, 478, 13L
- Kepner, J., Fan, X., Bahcall, N., Gunn, J.E., Lupton, R., & Xu, G. 1999, *ApJ*, 517, 78
- Kim, R.S.J., Strauss, M.A., Bahcall, N.A., Gunn, J.E., Lupton, R.H., Voges, W., Vogeley, M.S., & Schlegel, D. 1999, to appear in ASP Conf. Proc., Clustering at High Redshift, ed.s A. Mazure et al. (San Francisco: ASP), in press (astro-ph/9912302)
- Kodama, T. 1997, Ph.D. Thesis, University of Tokyo
- Kodama, T., Arimoto, N., Barger, A.J., & Aragón-Salamanca, A. 1998, *A&A*, 334, 99
- Kormendy, J. 1977, *ApJ*, 218, 333
- Ledlow, M.J., Loken, C., Burns, J.O., Owen, F.N., & Voges, W. 1999, *ApJ*, 516, 53L
- Lin, H., Yee, H.K.C., Carlberg, R.G., Morris, S.L., Sawicki, M., Patton, D.R., Wirth, G., & Shepherd, C.W. 1999, *ApJ*, 518, 533
- López-Cruz, O. 1997, Ph.D. Thesis, University of Toronto
- López-Cruz, O., & Yee, H.K.C. 2000a, submitted to *ApJ* (LCY00)
- López-Cruz, O., & Yee, H.K.C. 2000b, in preparation
- Lubin, L.M., Brunner, R., Metzger, M.R., Postman, M., & Oke, J.B. 2000, *ApJ*, 531, 5L
- Lubin, L.M. & Postman, M. 1996, *AJ*, 111, 1795
- Lubin, L.M., Postman, M., & Oke, J.B. 1998, *AJ*, 116, 643
- Lubin, L.M., Postman, M., Oke, J.B., Ratnatunga, K.U., Gunn, J.E., Hoessel, J.G., & Schneider, D.P. 1998, *AJ*, 116, 584
- Lucey, J.R. 1983, *MNRAS*, 204, 33
- Luppino, G.A., Gioia, I.M., Hammer, F., Le Fèvre, O., & Annis, J.A. 1999, *A&AS*, 136, 117
- Navarro, J.F., Frenk, C.S., & White, S.D.M. 1997, *ApJ*, 490, 493
- Oke, J.B., Postman, M., & Lubin, L.M. 1998, *AJ*, 116, 549
- Olsen, L.F., Scodreggio, M., da Costa, L., Slijkhuis, R., Benoist, C., Bertin, E., Deul, E., Erben, T., Guarnieri, M.D., Hook, R., Nonino, M., Prandoni, I., Wicenec, A., & Zaggia, S. 1999, *A&A*, 345, 363
- Oukbir, J. & Blanchard, A. 1997, *A&A*, 317, 1
- Pahre, M.A., Djorgovski, S.G., & de Carvalho, R.R. 1990, *ApJ*, 456, 79L
- Ponman, T.J., Cannon, D.B., & Navarro, J.F. 1999, *Nature*, 397, 135
- Postman, M., Lubin, L., Gunn, J.E., Oke, J.B., Hoessel, J.G., Schneider, D.P., & Christensen, J.A. 1996, *AJ*, 111, 615
- Postman, M., Lubin, L., & Oke, J.B. 1998, *AJ*, 116, 560
- Press, W.H., Teukolsky, S.A., Vetterling, W.T., & Flannery, B.P. 1992, *Numerical Recipes, The Art of Scientific Computing*, 2nd. edn., Cambridge, Cambridge University Press
- Rakos, K.D., Odell, A.P., & Schombert, J.M. 1997, *ApJ*, 490, 194
- Rakos, K.D. & Schombert, J.M. 1995, *ApJ*, 439, 47
- Rosati, P., Della Ceca, R., Norman, C., & Giacconi, R. 1998, *ApJ*, 492, 21L
- Sandage, A., Bingelli, B., & Tamman, G.A. 1985, *AJ*, 90, 1759
- Schade, D., Barrientos, L.F., & López-Cruz, O. 1997, *ApJ*, 477, 17L
- Schade, D., Carlberg, R.G., Yee, H.K.C., López-Cruz, O., & Ellingson, E. 1996, *ApJ*, 464, 63L
- Smail, I. & Dickinson, M. 1995, *ApJ*, 455, 99L
- Smail, I., Edge, A.C., Ellis, R.S., & Blandford, R.D. 1998, *MNRAS*, 293, 124
- Stanford, S.A., Elston, R., Eisenhardt, P.R., Spinrad, H., Stern, D., & Dey, A. 1997, *AJ*, 114, 2232
- Stanford, S.A., Eisenhardt, P.R., & Dickinson, M. 1998, *ApJ*, 492, 461 (SED98)
- Tadros, H., Efsthathiou, G., & Dalton, G. 1998, *MNRAS*, 296, 995
- Thompson, L.A. 1986, *ApJ*, 306, 384
- van Dokkum, P.G. & Franx, M. 1996, *MNRAS*, 281, 985
- van Dokkum, P.G., Franx, M., Kelson, D.D., & Illingworth, G.D. 1998, *ApJ*, 504, 17L
- van Haarlem, M.P., Frenk, C.S., & White, S.D.M. 1997, *MNRAS*, 287, 817
- Vikhlinin, A., McNamara, B.R., Forman, W., Jones, C., Quintana, H., & Hornstrup, A. 1998, *ApJ*, 503, 77
- Vio, R., Fasano, G., Lazzarin, M., & Lessi, O. 1994, *A&A*, 289, 640
- Williams, J.P., de Geus, E.J., & Blitz, L. 1994, *ApJ*, 451, 252
- Yee, H.K.C., Gladders, M.D., & López-Cruz, O. 1999, in ASP Conf. Proc. 191, Photometric Redshifts and High Redshift Galaxies (San Francisco: ASP), 166
- Yee, H.K.C., Morris, S.L., Lin, H., Carlberg, R.G., Hall, P.B., Sawicki, M., Patton, D.R., Wirth, G.D., Ellingson, E., & Shepherd, C.W. 2000a, *ApJS*, in press
- Yee, H.K.C., Ellingson, E., Morris, S.L., & Carlberg, R.G. 2000b, in preparation

Ziegler, B.L. & Bender, R. 1997, MNRAS, 291, 527

Ziegler, B.L., Saglia, R.P., Bender, R., Belloni, P., Greggio, L.,  
& Seitz, S. 1999, A&A, 346, 13

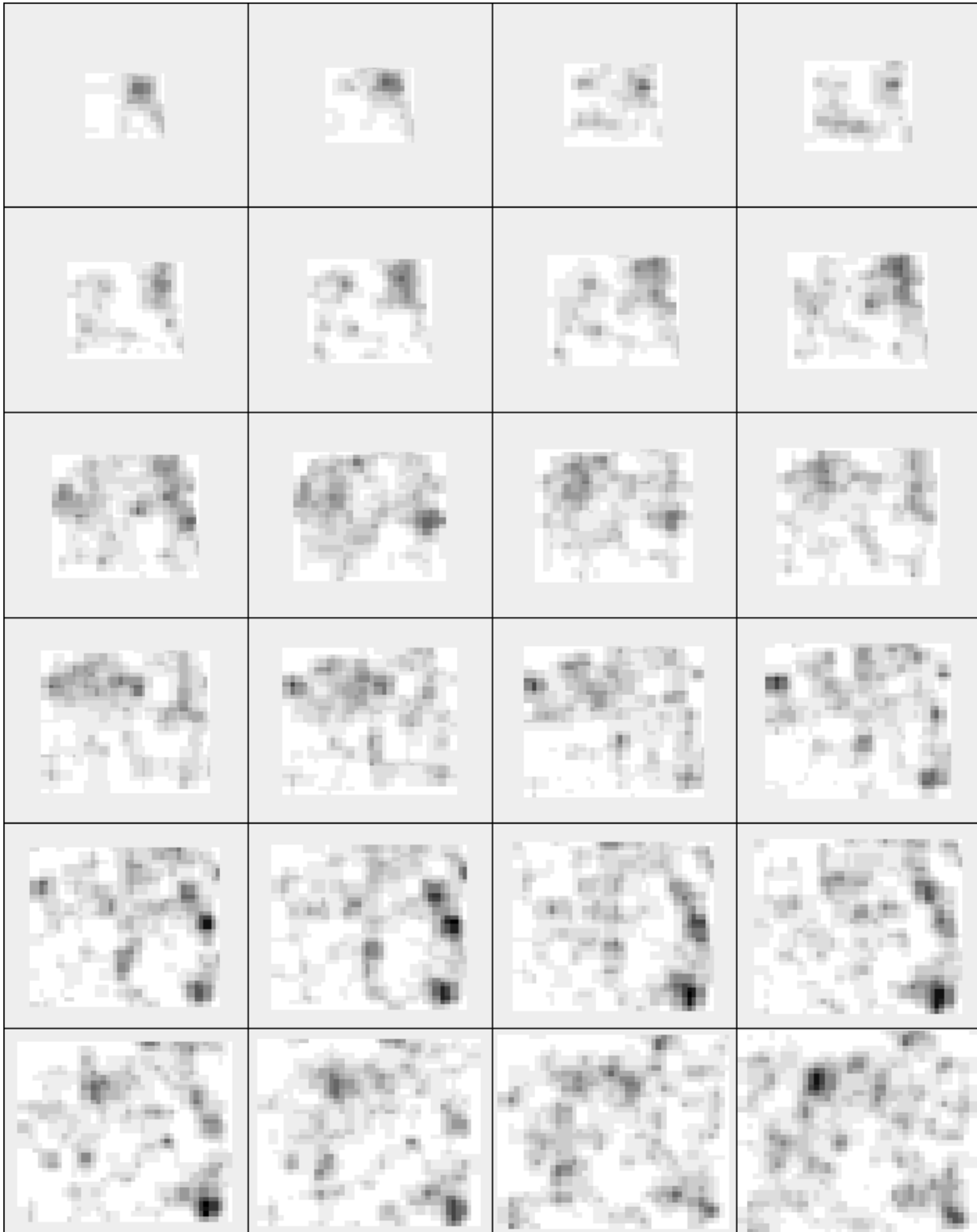


Fig. 8.— The individual maps of  $\sigma_{ij}$  from the patch CNOC0223+00. Grayscale levels from white to black correspond to values of  $0 < \sigma_{ij} < 5$  in the normalized maps. The central redshift of the slices runs from  $z \sim 0.1$  to  $z \sim 0.6$ , from the top left to bottom right. The maps are displayed at all redshifts with the same pixel scale of  $0.125 h^{-1}$  proper Mpc. The significant peaks in the last two rows are discussed in more detail in the text and Figure 9.

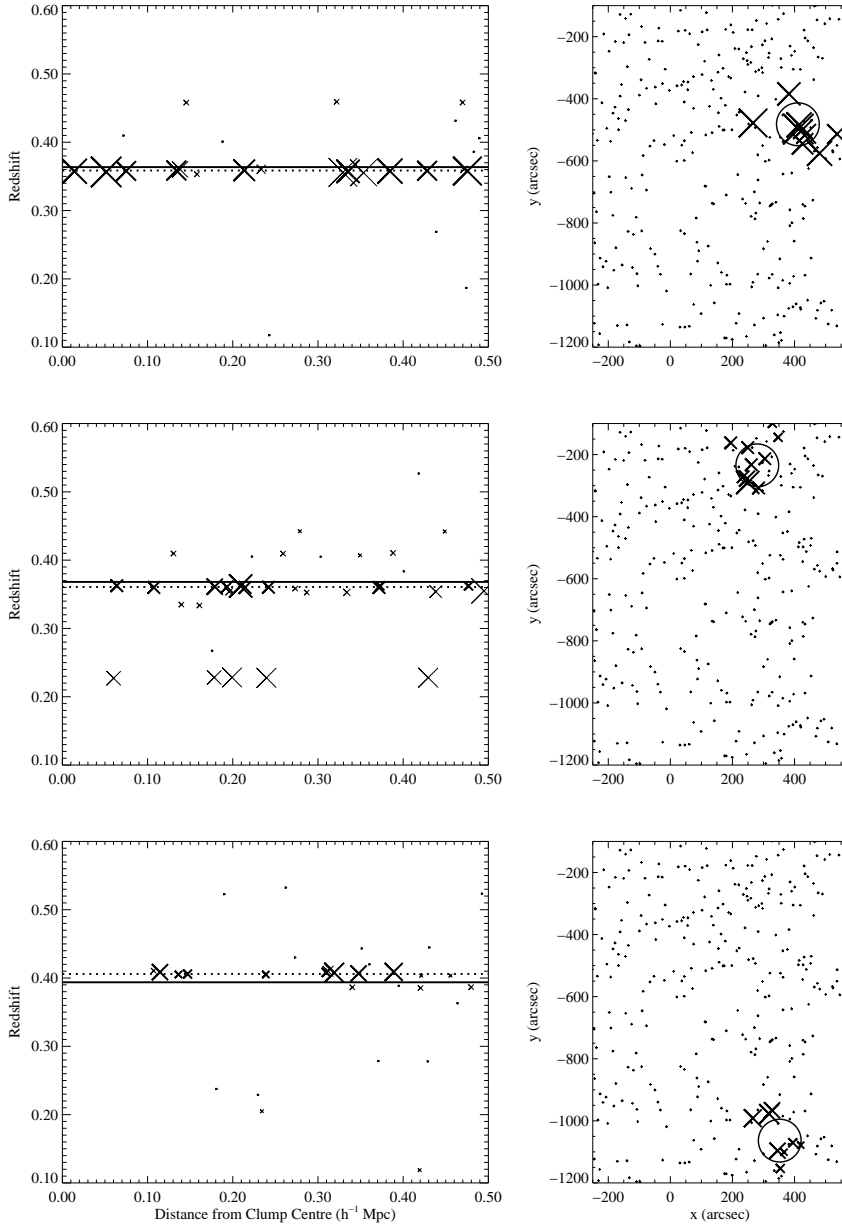


Fig. 9.— Example candidate clusters from the CNOC2 database found by the CRS method and identified with real redshift structures. The right hand panels show the  $x$ - $y$  plots of all galaxies in the region with measured redshifts (small pluses, same region in each panel). Galaxies taken to be associated with the peak under consideration are given by large heavy crosses, with the projected  $x$ - $y$  position of the CRS peak marked by a circle. The panels on the left show the redshift vs. distance from this projected peak center for galaxies (crosses) near each candidate. Symbol sizes are proportional to the number of ‘friends’ each galaxy has in the redshift sample. In each, the predicted redshift from the CRS peak is shown as a horizontal line, and the computed mean spectroscopic redshift of the group identified from the redshift catalog is shown as a dashed line. The heavy symbols indicate galaxies taken to be associated with that overdensity. Note that the CRS method successfully separated two galaxy groups with close proximity in both projected angular (4.5 arcmin, or  $0.9 h^{-1}$  Mpc) and velocity ( $\sim 1750 \text{ km s}^{-1}$ ) space.